Noname manuscript No.
(will be inserted by the editor)

Axisymmetric diffusion kurtosis imaging with Rician bias correction: A simulation study

Jan Malte Oeschger[a] · **Karsten Tabelow**[b] · **Siawoosh Mohammadi**[a,c]

Received: / Accepted: date

Abstract
Purpose: To compare the estimation accuracy of axisymmetric diffusion kurtosis imaging (DKI) and standard DKI in combination with Rician bias correction (RBC) under the influence of noise.
Methods: Axisymmetric DKI is more robust against noise-induced variation in the measured signal than standard DKI because of its reduced parameter space. However, its susceptibility to Rician noise bias at low signal-to-noise ratios (SNRs) is unknown. We investigate estimation accuracy of standard DKI and axisymmetric DKI on five axisymmetric DKI tensor metrics (AxTM): the parallel and perpendicular diffusivity and kurtosis and the mean kurtosis. Estimation accuracy was investigated in a simulation study based on two datasets. One dataset consists of synthetic data of tissues of varying degrees of fiber alignment and the other one is based on in-vivo data of typical white matter fiber tracts. Furthermore, the influence of RBC on axisymmetric DKI is investigated.

Results: We found that RBC was most effective for increasing accuracy of the parallel AxTM in anisotropic white matter. For the perpendicular AxTM, axisymmetric DKI without RBC performed slightly better than with RBC. However, the combination of axisymmetric DKI with RBC was the overall best performing algorithm across all five AxTM and the axisymmetric DKI framework itself substantially improved parameter estimation in tissues with low fiber alignment.
Conclusion: The combination of axisymmetric DKI with RBC facilitates accurate DKI parameter estimation at unprecedented low SNRs (≈ 15), possibly making it a valuable tool for neuroscience and clinical research studies where scan time is a limited resource. The tools used in this paper for time-efficient estimation of the AxTM with axisymmetric DKI, standard DKI and RBC are available in the open-source ACID toolbox for SPM.

Keywords Axisymmetric DKI, Rician bias correction, SNR, Microscopic fiber alignment, Simulation

[a]University Medical Center Hamburg Eppendorf, Institute of Systems Neuroscience, Hamburg, Germany

[b]Weierstrass Institute for Applied Analysis and Stochastics, Berlin, Germany

[c]Max Planck Institute for Human Cognitive and Brain Sciences, Department of Neurophysics, Leipzig, Germany

Glossary

RBC Rician bias correction.
DTI Diffusion tensor imaging.
DKI Diffusion kurtosis imaging.
HA Fiber with high alignment.
MA Fiber with moderate alignment.
LA Fiber with low alignment.
AxTM Axisymmetric DKI tensor metrics: $D_\parallel$, $D_\perp$, $W_\parallel$, $W_\perp$, and $\overline{W}$.
$D_\parallel$ Parallel diffusivity.
$D_\perp$ Perpendicular diffusivity.
$W_\parallel$ Parallel kurtosis.
$W_\perp$ Perpendicular kurtosis.
$\overline{W}$ Mean kurtosis.

1 Introduction

Diffusion weighted MRI is an in-vivo imaging modality used in neuroscience and clinical research. It is sensitive to changes in nervous tissues that, e.g., go along with neurodegenerative diseases like epilepsy and multiple sclerosis (Deppe et al., 2008; Rovira et al., 2015). Diffusion MRI measures the net diffusion of nuclear spins of hydrogen nuclei in water molecules that are omnipresent in nervous tissue.

Diffusion of water molecules within the microstructural tissue landscape can be arbitrarily complex. A data-efficient method that captures both, standard Gaussian diffusion and more complex restricted diffusion processes (e.g., due to diffusion of water trapped in the cell-body of axons), is the recently introduced axisymmetric diffusion kurtosis imaging (DKI) framework (Hansen et al., 2016; Hansen and Jespersen, 2017). Its data-efficiency stems from requiring fewer diffusion weighted images than standard DKI, for the following reasons: while standard diffusion kurtosis imaging (DKI) is based on 22 parameters (Jensen et al., 2005), axisymmetric DKI has a reduced parameter space of 8 parameters due to imposing the assumption of axisymmetrically distributed axons. This is likely a reasonable assumption in major white matter fiber bundles (Hansen et al., 2016). Furthermore, this is expected to make axisymmetric DKI less susceptible to the noise induced variation of the acquired diffusion MRI signals.

Noise in MRI images introduces a random variation into the measured diffusion signals (Derek K. Jones, 2012) and a bias for the estimated DKI parameters when the signal-to-noise-ratio (SNR) is low. This bias is known as the "Rician noise bias" (Gudbjartsson and Patz, 1995; Glenn et al., 2015) and becomes more severe, the lower the SNR is. Diffusion MRI is prone to a low SNR (Derek K. Jones, 2012) because it generates image contrast from additional spin dephasing associated with water mobility leading to a signal attenuation. DKI is even more susceptible to the Rician noise bias compared to conventional diffusion tensor imaging (DTI), since estimating the DKI parameters requires multiple diffusion shells including higher diffusion weighting, lowering the SNR. This increases the demand for effective Rician bias correction (RBC) schemes (Henkelman, 1985; Sijbers et al., 1998) in DKI. Right now it is unclear whether fitting the axisymmetric DKI framework with its reduced parameter space (axisymmetric DKI has 8 parameters while standard DKI has 22) is better suited for parameter estimation from noisy diffusion MRI data than standard DKI. And it is furthermore unknown, how this could affect the susceptibility to the Rician noise bias.

The effect of the Rician noise bias on the fractional anisotropy (FA), mean diffusivity (MD) and mean kurtosis $\overline{W}$ was shown to be mitigated by using RBC in standard DKI (Koay et al., 2009; Veraart et al., 2011, 2013a; André et al., 2014). Of these three parameters, only the mean kurtosis is part of the axisymmetric DKI tensor metrics (AxTM). The AxTM are the parallel and perpendicular diffusivities ($D_{\parallel}$ and $D_{\perp}$) and the mean, parallel, and perpendicular kurtosis ($\overline{W}$, $W_{\parallel}$ and $W_{\perp}$). Here parallel and perpendicular are in reference to the axis of symmetry. The axisymmetric DKI framework contains three additional parameters, the two angles of the unit vector pointing along the axis of symmetry, and the non diffusion-weighted signal ($b = 0$).

The AxTM can be estimated based on standard DKI where they are computed as aggregates from its 22 parameters or directly with axisymmetric DKI (see Table 2.1). The AxTM are of particular interest for neuroscience and clinical research (Coutu et al., 2014; Cox et al., 2016; Elliott et al., 2018; Genç et al., 2018; Karolis et al., 2019; Donat et al., 2021) because they are invariant against coordinate transformations and describe free and restricted diffusion within nervous tissue. Furthermore, the AxTM can be directly related to the tissue microstructure. The latter relation is established via their mathematical relation to the five microstructure parameters of the biophysical standard model (Novikov et al., 2018; Jespersen et al., 2018): axon water fraction, axon dispersion, and three diffusivities associated with the intra- and extra-axonal space.

Furthermore, it can be expected that RBC will impact the estimation of the parallel and perpendicular AxTM differently because they are associated with different levels of water mobility and consequently different levels of SNR. Another open question is the influence of fiber alignment on the effectiveness of RBC. It can be expected that the degree of fiber alignment within a white matter MRI voxel affects water mobility and thereby also the efficiency of RBC.

The aim of this work is to compare the estimation accuracy of both standard DKI and axisymmetric DKI in combination with RBC. Motivated by the improved parameter estimation accuracy when applying RBC in standard DKI, we investigate whether RBC improves accuracy of axissymmetric DKI on all five AxTM. In particular, we investigate the hypothesis that the per-

formance of RBC depends on whether parallel or perpendicular AxTM are estimated and also investigate the influence of the degree of fiber alignment, as both factors affect water mobility and hence increase severity of the Rician noise bias. To study these questions, we simulated two datasets: the "`synthetic dataset`" is based on three sets of synthetic AxTM describing tissues with varying degrees of fiber alignment which allows us to assess AxTM estimation accuracy as a function of fiber alignment; the "`in-vivo like dataset`" is based on in-vivo measurements of white matter tissue fiber tracts with a high to moderate fiber alignment which allows us to study AxTM estimation accuracy under realistic, in-vivo like conditions. In both studies, axisymmetric DKI and standard DKI (with and without RBC) were used to obtain estimates of the five AxTM.

2 Methods

2.1 Standard DKI signal representation

For a given diffusion weighting b and diffusion gradient $\vec{g} = (g_1, g_2, g_3)^\mathsf{T}$, the noise-free DKI signal can be represented as Jensen and Helpern (2003); Jensen et al. (2005):

$$\eta_{b,\vec{g}}(\eta_0, D, W) = \eta_0 \exp\left[-bD + \frac{b^2}{6}\left(\frac{\mathrm{Tr}(D)}{3}\right)^2 W\right] \tag{2.1a}$$

$$D = \sum_{i,j=1}^{3} g_i g_j D_{ij} \tag{2.1b}$$

$$W = \sum_{i,j,k,l=1}^{3} g_i g_j g_k g_l W_{ijkl} \tag{2.1c}$$

where D_{ij} are the diffusion tensor entries, W_{ijkl} are the kurtosis tensor entries and η_0 is the non-diffusion-weighted signal ($b = 0\frac{\mathrm{s}}{\mathrm{mm}^2}$).

2.2 Axisymmetric DKI

Axisymmetric DKI (Hansen et al., 2016) assumes symmetric diffusion around an axis of symmetry $\vec{c}$ inside an imaging voxel. Mathematically, this assumption leads to axisymmetric diffusion and kurtosis tensors with a drastically reduced number of independent tensor parameters compared to standard DKI (from 15 to 3 parameters for the kurtosis tensor and from 6 to 2 parameters for the diffusion tensor). The symmetry assumptions are likely to be a reasonable approximation to diffusion in major white matter fiber bundles (Hansen et al., 2016) due to their structural organization.

With the axis of symmetry $\vec{c}$ parameterized by the inclination θ and azimuth ϕ: $\vec{c} = \begin{pmatrix} \sin\theta\cos\phi \\ \sin\theta\sin\phi \\ \cos\theta \end{pmatrix}$, the diffusion and kurtosis tensors can be determined according to Hansen et al. (2016):

$$D = D_\parallel \mathbf{I} + (D_\parallel - D_\perp)\vec{c}\vec{c}^T \tag{2.2}$$

and

$$W = \frac{1}{2}(10W_\perp + 5W_\parallel - 15\overline{W})\mathbf{P} + W_\perp \Lambda + \frac{3}{2}(5\overline{W} - W_\parallel - 4W_\perp)\mathbf{Q}$$

where $\Omega = \{D_\parallel, D_\perp, W_\parallel, W_\perp, \overline{W}, \eta_0, \theta, \phi\}$ are the 8 framework's parameters (η_0 is the non diffusion-weighted signal) and $\mathbf{I} = \begin{pmatrix} 1 & 0 & 0 \\ 0 & 1 & 0 \\ 0 & 0 & 1 \end{pmatrix}$ is the identity matrix. The tensors $\mathbf{P}, \Lambda$ and $\mathbf{Q}$ can be computed with the Kronecker delta δ_{xy} and the components of the axis of symmetry c_x $(x, y \in 1, 2, 3)$ as: $\mathbf{P}_{ijkl} = c_i c_j c_k c_l$, $\mathbf{Q}_{ijkl} = \frac{1}{6}(c_i c_j \delta_{kl} + c_i c_k \delta_{jl} + c_i c_l \delta_{jk} + c_j c_k \delta_{il} + c_j c_l \delta_{ik} + c_k c_l \delta_{ij})$ and $\Lambda_{ijkl} = \frac{1}{3}(\delta_{ij}\delta_{kl} + \delta_{ik}\delta_{jl} + \delta_{il}\delta_{jk})$ (Hansen et al., 2016). The according noise-free signal $\eta_{b,\vec{g}}(\Omega)$ can then be computed based upon the axissymmetric tensors (Hansen et al., 2017):

$$\eta_{b,\vec{g}}(\Omega) = \eta_0 \exp\left(-B_{ij}D_{ij} + \frac{1}{6}\overline{D}^2 B_{ij}B_{kl}W_{ijkl}\right) \tag{2.3}$$

where

$$B_{ij}D_{ij} = \mathrm{Tr}(B)D_\perp + (D_\parallel - D_\perp)\vec{c}^T B\vec{c} \tag{2.4}$$

and

$$\begin{aligned} B_{ij}B_{kl}W_{ijkl} = &\frac{1}{2}(10W_\perp + 5W_\parallel - 15\overline{W})(\vec{c}^T B\vec{c})^2 \\ &+ \frac{1}{2}(5\overline{W} - W_\parallel - 4W_\perp)(\vec{c}^T B\vec{c}\,\mathrm{Tr}(B) \\ &+ 2\vec{c}^T BB\vec{c}) + \frac{W_\perp}{3}(Tr(B)^2 + 2\,\mathrm{Tr}(B \otimes B)) \end{aligned}$$

with $B = b\begin{pmatrix} g_x^2 & g_x g_y & g_x g_z \\ g_x g_y & g_y^2 & g_y g_z \\ g_x g_z & g_y g_z & g_z^2 \end{pmatrix}$.

The AxTM can be computed from the standard DKI tensor metrics assuming axial-symmetry. For example, $D_\perp = \frac{\lambda_2 + \lambda_3}{2}$ where λ refers to the eigenvalues of the

diffusion tensor. Formulas for the computation of the other AxTM can be found in Tabesh et al. (2011), Table 2.1 shows the AxTM and the standard DKI tensor metrics needed to compute them. Fig. 2.1 shows the five AxTM obtained with the axisymmetric DKI fit without RBC available in the open source ACID toolbox for SPM.

2.3 Parameter estimation and the Rician noise bias

Standard DKI or axisymmetric DKI parameter estimation would typically be done using the acquired magnitude signals $S_{b,\vec{g}}$ and Eq. (2.1a) or Eq. (2.3) in the least-squares approach (Veraart et al., 2013b; Tabesh et al., 2011):

$$(\eta_0, \hat{D}, \hat{W}) = \arg\min \eta_0, D, W \sum_i (S_{b,\vec{g_i}} - \eta_{b,\vec{g_i}}(\eta_0, D, W))^2 \tag{2.5}$$

However, this least-squares approach is built on the assumption of Gaussian distributed noise in $S_{b,\vec{g_i}}$ which is not true in reality. $S_{b,\vec{g}}$ is a magnitude signal computed from the noise contaminated k-space data described by a complex Gaussian (standard deviation σ) as the sum of squares of the measured signal intensity (Constantinides et al., 1997) from the receiver coil after it was Fourier transformed into real space. Computing the sum of squares rectifies the composite magnitude signal and leads to Rician distributed noise for one receiver coil (L= 1). Therefore, assuming Gaussian noise in MRI magnitude signals leads to a bias that propagates into the estimated parameters which is referred to as the "Rician noise bias". Eq.(2.5) is therefore biased.

More generally, if one assumes uncorrelated noise and statistically independent receiver coils with an equivalent noise variance (Aja-Fernández and Tristán-Vega, 2012), the resulting probability density function of the noisy magnitude data is given by a non-central χ-distribution (Constantinides et al., 1997), where $2L$ is the number of degrees of freedom of the distribution. $L = 1$ results in the Rician distribution (Rice, 1944; Gudbjartsson and Patz, 1995).

The severity of the Rician noise bias depends on the SNR (Polzehl and Tabelow, 2016) because the sum of squares rectifies the composite magnitude signal: the lower the SNR, the larger the bias. For RBC, we rely on an approach outlined in Polzehl and Tabelow (2016) that uses the expectation value $\mathbf{E}(S_{b,\vec{g}})$ of the composite magnitude signal. The probability density function of $\mathbf{E}(S_{b,\vec{g}})$ is a non-central χ distribution and given by (Polzehl and Tabelow, 2016):

$$\mathbf{E}(S_{b,\vec{g}}) = \mu(\eta_{b,\vec{g}}(\eta_0, D, W), \sigma) = \sigma\sqrt{\frac{\pi}{2}} \cdot \mathbf{L}_{1/2}^{(L-1)}\left(\frac{\eta_{b,\vec{g}}(\eta_0, D, W)^2}{2\sigma^2}\right) \tag{2.6}$$

where $\frac{\eta_{b,\vec{g}}(\eta_0,D,W)}{\sigma}$ is the SNR and $\mathbf{L}_{1/2}^{(L-1)}(x) = \frac{\Gamma(L+1/2)}{\Gamma(3/2)\Gamma(L)}\mathbf{M}(-1/2, L, x)$ is the generalized Laguerre polynomial which can be expressed using a confluent hypergeometric function $\mathbf{M}$ and the Gamma function Γ. Only for simplicity of notation, in the text we neglect any possible dependence of σ on b, $\vec{g}$ or location, the employed RBC algorithm used the same σ in every image voxel. The SNR dependent expectation value Eq. (2.6) differs from the noise-free signal, $\mu(\eta_{b,\vec{g}}(\eta_0, D, W), \sigma) > \eta_{b,\vec{g}}(\eta_0, D, W)$ with the difference decreasing with increasing SNR. Following Polzehl and Tabelow (2016), we implemented a time-efficient fitting algorithm that, unlike Eq. (2.5), accounts for Rician noise in magnitude MRI data by solving the optimization problem:

$$(\hat{\eta_0}, \hat{D}, \hat{W}) = \text{argmin}_{\eta_0, D, W} \sum_i (S_{b,\vec{g_i}} - \mu(\eta_{b,\vec{g_i}}(\eta_0, D, W), \sigma))^2 \tag{2.7}$$

Estimating parameters this way is referred to as "quasi-likelihood" estimation and is denoted as "RBC ON" in this paper. It was shown, that parameter estimation using the non-central χ noise statistic in a quasi-likelihood framework yields asymptotically unbiased parameter estimates (Bunke and Schmidt, 1980; Polzehl and Tabelow, 2016).

Rician bias corrected, standard DKI or axisymmetric DKI parameter estimation can be done by using Eq. (2.1a) or Eq. (2.3) to compute the noise-free signal predictions $\eta_{b,\vec{g}}$, then using Eq. (2.6) to compute $\mu(\eta_{b,\vec{g}}(\eta_0, D, W), \sigma)$ and finally minimize Eq. (2.7) to estimate the framework parameters (η_0, D, W) for standard DKI or Ω for axisymmetric DKI.

In reality, noise correlations between receiver coils occur and are non-negligible, especially for a higher number of receiver coils (32 or 64). This affects the degrees of freedom of the underlying noise statistic. However, the non-central χ distribution can still be used as a good approximation, if an effective number of coils L_{eff} and noise variance σ^2_{eff} are used (Aja-Fernández and

Table 2.1: AxTM and standard DKI tensor metrics with which they are calculated. The numbers show how many standard DKI tensor metrics are needed to compute the AxTM. λ refers to the eigenvalues of the diffusion tensor, W refers to the components of the kurtosis tensor.

Axisymmetric DKI tensor metric (AxTM)	Corresponding standard DKI tensor metrics
$D_{\parallel}$	1: λ_1
$D_{\perp}$	2: λ_2, λ_3
$W_{\parallel}$	4: λ_1, λ_2, λ_3, W_{1111}
$W_{\perp}$	6: λ_1, λ_2, λ_3, W_{2222}, W_{3333}, W_{2233}
$\overline{W}$	9: λ_1, λ_2, λ_3, W_{1111}, W_{2222}, W_{3333}, W_{2233}, W_{1133}, W_{1122}

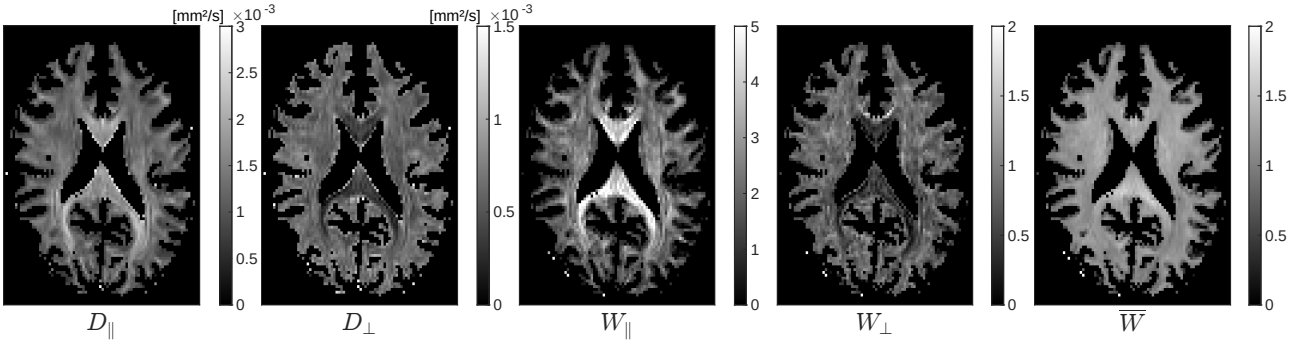

Fig. 2.1: AxTM results in white matter. The AxTM are the parallel and perpendicular diffusivity and kurtosis and the mean kurtosis. The shown maps were obtained with the axisymmetric DKI fit available in the open source ACID toolbox for SPM that was used in this work. The AxTM were estimated from the in-vivo measurement used for the `in-vivo like dataset` (Figure 2.3).

Tristán-Vega, 2012) for which $L \geq L_{\text{eff}}$ and $\sigma^2 \leq \sigma^2_{\text{eff}}$ can be shown. Similarly, the generalized autocalibrating partially parallel acquisition (GRAPPA) scheme can be accounted for by specifying an effective number of coils L_{eff}, while $L = 1$ for sensitivity encoding (SENSE) (Aja-Fernández and Tristán-Vega, 2012).

2.4 Parameter estimation with the Gauss-Newton algorithm

To minimize Eq. (2.5) or Eq. (2.7), we have implemented a Gauss-Newton minimization algorithm (Modersitzki, 2009) in Matlab for time-efficient, slice-wise and parallelizable parameter estimation on MR-images. It is freely available online within the ACID toolbox (http://www.diffusiontools.com/) for SPM. Slice-wise fitting refers to fitting all voxels of an image-slice at the same time which improves run-time. The implemented algorithm is highly adaptable and can fit any signal model (especially non-linear models). Gauss Newton parameter estimation approximates the search direction in parameter space based on the Jacobian and is sensitive to the initial guess.

2.5 Simulation study: Datasets and overview

We assessed estimation accuracy of the five AxTM as a function of the SNR in a simulation study with two types of datasets. One dataset consisted of three synthetic voxels with varying fiber alignment (defined in Coelho et al. (2019)). This dataset is refereed to as `"synthetic dataset"` because it was derived in the context of another study (Coelho et al., 2019) by random sampling of the parameter space of biophysical parameters and consequent derivation of the corresponding AxTM. The other dataset consisted of twelve major white matter fiber tract voxels from an in-vivo brain measurement, this dataset is refereed to as `"in-vivo like dataset"`. Details on both datasets are listed below and in Figure 2.2. For both datasets, magnitude diffusion MRI data were simulated for varying SNRs and fitted with standard DKI and axisymmetric DKI, with and without RBC (as described in Section 2.3) to obtain estimates of the five AxTM. Accuracy of the obtained AxTM estimates were evaluated as the mean absolute percentage error (MAPE):

$$\text{MAPE} = 100 \cdot \frac{\mid \text{GT} - \overline{\text{FitResults}}(\text{SNR}) \mid}{\text{GT}} \tag{2.8}$$

Here GT reefers to the ground truth and $\overline{\text{FitResults}}$ reefers to the average of the fit results over the noise

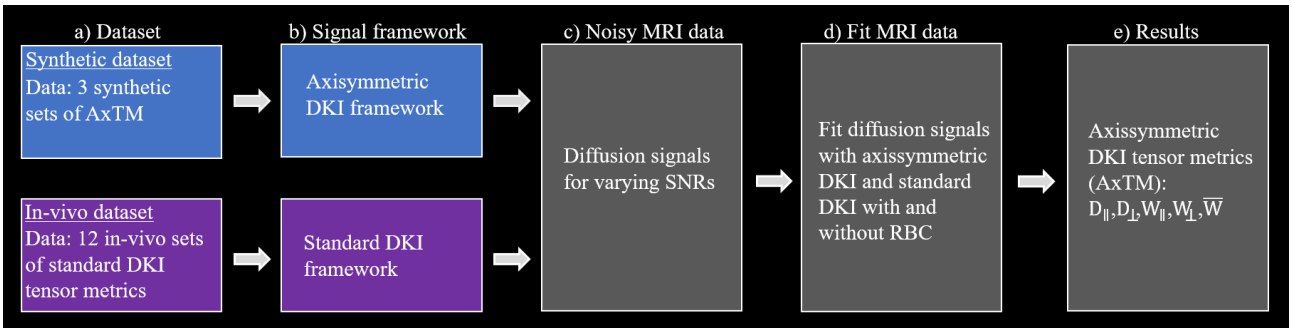

Fig. 2.2: Scheme of the simulation study. Simulations were performed in 5 steps: a) choice of datasets, b) signal framework used for simulation, c) diffusion signal simulation and contamination with noise, d) parameter estimation and e) results. Note that both simulation studies only differed in a) and b) but were identical in the following procedures. a) the `synthetic dataset` consisted of 3x5 sets of AxTM (Table 7.3) while the `in-vivo like dataset` consisted of 12x22 standard DKI tensor metrics (Table 7.1 in the Supplementary material). b) The DKI signal framework used for diffusion signal simulation. c) Diffusion signal data were contaminated with 2500 Rician noise samples for each SNR=$[1, 2, 3...100]$. d) Simulated diffusion data were fitted with axisymmetric DKI and standard DKI with and without RBC in both simulation studies for each of the 2500 noise samples. e) The axisymmetric DKI tensor metrics (AxTM): $D_{\parallel}$, $D_{\perp}$, $W_{\parallel}$, $W_{\perp}$ and $\overline{W}$ were calculated for standard DKI data (for axisymmetric DKI they were directly estimated), averaged across the 2500 noise samples per SNR and finally compared to the ground truth.

samples. We evaluated the accuracy of the AxTM estimates for each estimation method by looking for the SNR after which the MAPE was smaller 5%. The 5% threshold was considered an acceptable error in a trade-off between estimation accuracy and SNR requirement. The different setup of both simulation studies enables an isolated investigation of the effectiveness and tissue dependence of the RBC and to test the fitting methods in an `in-vivo like dataset`. As a summary to compare each method, we looked at the maximum SNR needed across the five AxTM for which MAPE consistently $< 5\%$ for all AxTM ("Maximum" column in Fig. 3.2).

Datasets: The `synthetic dataset` consisted of three synthetic sets of AxTM (from Coelho et al. (2019)) describing three voxels with varying fiber alignment, one with fibers with low alignment ("LA", FA=0.067), one with fibers with moderate alignment ("MA", FA=0.24) and one with highly aligned fibers ("HA", FA=0.86). The AxTM of the three synthetic voxels are summarized in Table 7.3 ("Supplementary material"). Figure 2.4 shows two areas of typical brain regions in a map of the mean kurtosis $\overline{W}$ where LA and HA voxels can be found and the corresponding idealized fiber stick model.

The `in-vivo like dataset` consists of twelve voxels extracted from four major white matter tracts (three voxels from each of the four fiber tracts, see Figure 2.3) from an in-vivo brain measurement (SNR=23.4) of a healthy volunteer. The twelve voxels were extracted from the in-vivo measurement by fitting the standard DKI framework in 12 voxels to get the corresponding 22 standard DKI tensor metrics, the derived data are therefore refereed to as "in-vivo like". Three voxels with moderately to highly aligned fibers (defined through their fractional anisotropy (FA)) were extracted from these four major white matter fiber tracts based upon the Jülich fiber atlas: the callosum body (`cb`), the corticospinal tract (`ct`), the optic radiation (`or`) and the superior longitudinal fasciculus (`slf`), see Figure 2.3. The sets of the 12 in-vivo like standard DKI tensor metrics are documented in the Supplementary material in Table 7.1, the derived AxTM are found in Table 7.2.

Signal framework used for simulation: The three synthetic voxels of AxTM were simulated with the axisymmetric DKI framework to first obtain noise-free diffusion MRI magnitude signals. The twelve in-vivo like voxels were simulated with the standard DKI framework to first obtain noise-free diffusion MRI magnitude signals.

Contamination with noise: For both the synthetic and the `in-vivo like dataset`, the noise-free diffusion MRI magnitude signals were contaminated with noise for SNRs $[1, 2, 3...100]$.

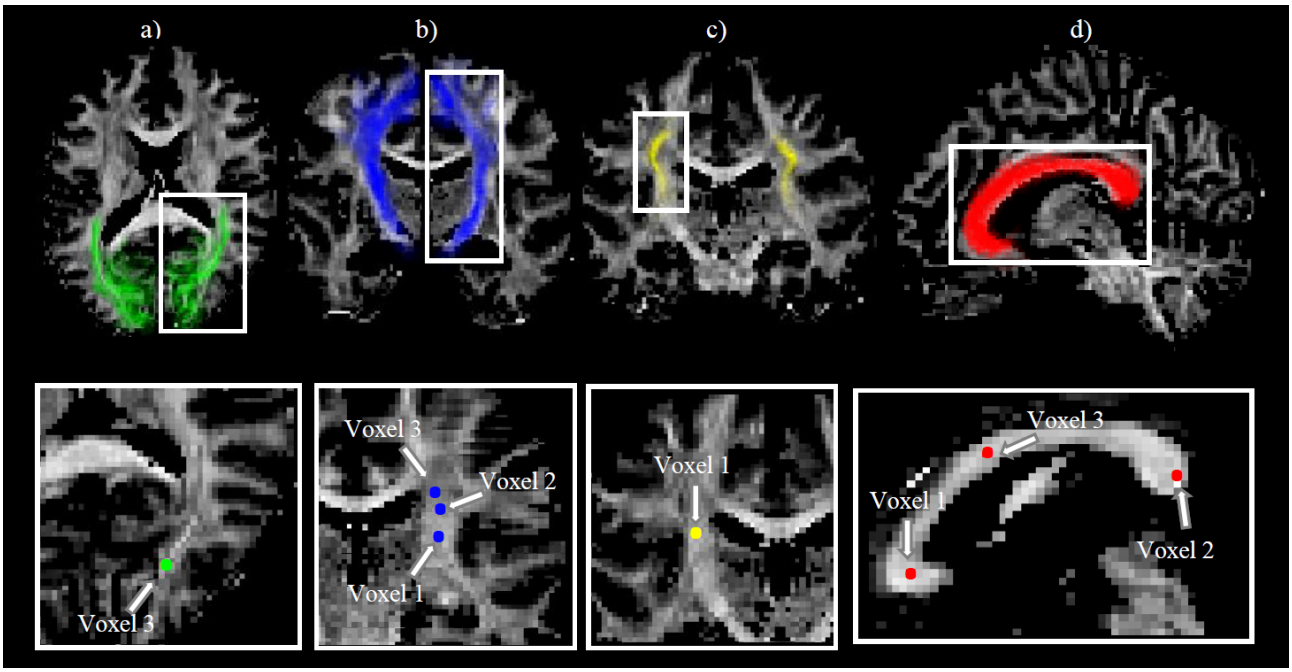

Fig. 2.3: Selection of voxels of the `in-vivo like dataset`: The four white matter fiber pathways within which voxels were selected and used as a basis for the `in-vivo like dataset`. Top: a) Optic radiation (or), b) cortico spinal tract (ct), c) superior longitudinal fasciculus (slf) and d) callosum body (cb) in a fractional anisotropy (FA) map of a healthy human brain. The fiber pathways were identified with the coregistered Jülich fiber atlas (Eickhoff et al., 2005). Bottom: Voxels in the fiber pathways used for the `in-vivo like dataset`. In each fiber pathway, three voxels were chosen for the `in-vivo like dataset` (for slf an or only one is shown here because the chosen voxels were not in the same slice).

Estimating the five AxTM: Both, the simulated signals from the `synthetic` and the `in-vivo like dataset` were fitted with axisymmetric DKI and standard DKI, with and without RBC (section 2.3) to obtain estimates of the AxTM whose accuracy could then be investigated as a function of SNR.

2.6 In-vivo data acquistion and simulated sequence

The DWI sequence used to acquire the `in-vivo like dataset` was a mono-polar single-shot spin-echo EPI scheme, consisting of 16 non-diffusion-weighted images ($b = 0$ image). The diffusion weighted images were acquired at three b values ($500\frac{\mathrm{s}}{\mathrm{mm}^2}$, $1250\frac{\mathrm{s}}{\mathrm{mm}^2}$, $2500\frac{\mathrm{s}}{\mathrm{mm}^2}$), sampled for 60 unique diffusion-gradient directions for the $1250\frac{\mathrm{s}}{\mathrm{mm}^2}$ and $2500\frac{\mathrm{s}}{\mathrm{mm}^2}$ shells and 30 unique directions for the $500\frac{\mathrm{s}}{\mathrm{mm}^2}$ shell. The entire protocol was repeated with reversed phase encoding directions ("blip-up", "blip-down" correction) to correct for susceptibility-related distortions so that in total $166 \cdot 2$ images were acquired. Other acquisition parameters were: an isotropic voxel size of ($1.6\mathrm{mm}^3$), FoV of $240\mathrm{x}230\mathrm{x}154\mathrm{mm}^3$, TE = 73ms, TE = 5300ms and 7/8 partial Fourier imaging. Signal simulation in our simulation study was done with only one $b = 0$ signal, so that the simulated sequence consisted of 151 signals per noise realization.

2.7 Simulation studies: Details

We simulated 100 SNRs: SNR $= [1, 2, 3, ...100]$. Noise was added according to $\mathrm{S}_{\mathrm{cont}} = |\mathrm{S}_{\mathrm{noise-free}} + \alpha + \beta i|$, where $\alpha, \beta \in \mathcal{N}(0, \sigma)$ are drawn from a zero mean Gaussian with standard deviation σ, yielding different SNR $= \sqrt{2}\frac{S_0}{\sigma}$ (for one receiver coil) for a given $S_0 = 1$. For every SNR, 2500 noise samples were realized, i.e., $2500 \cdot 151$ pairs (α, β) were drawn and $2500 \cdot 151$ $\mathrm{S}_{\mathrm{cont.}}$ were calculated per SNR for every simulated voxel. These diffusion MRI magnitude signals were then fitted with the four proposed methods (section 2.3). For each of the 2500 noise samples per SNR, 2500 parameter estimates of $D_{\|}, D_{\perp}, W_{\|}, W_{\perp}, \overline{W}$ were obtained and averaged to find the SNR above which the average over these 2500 noise samples had a MAPE $<$ 5% (`synthetic datset`). For the `in-vivo datset` this

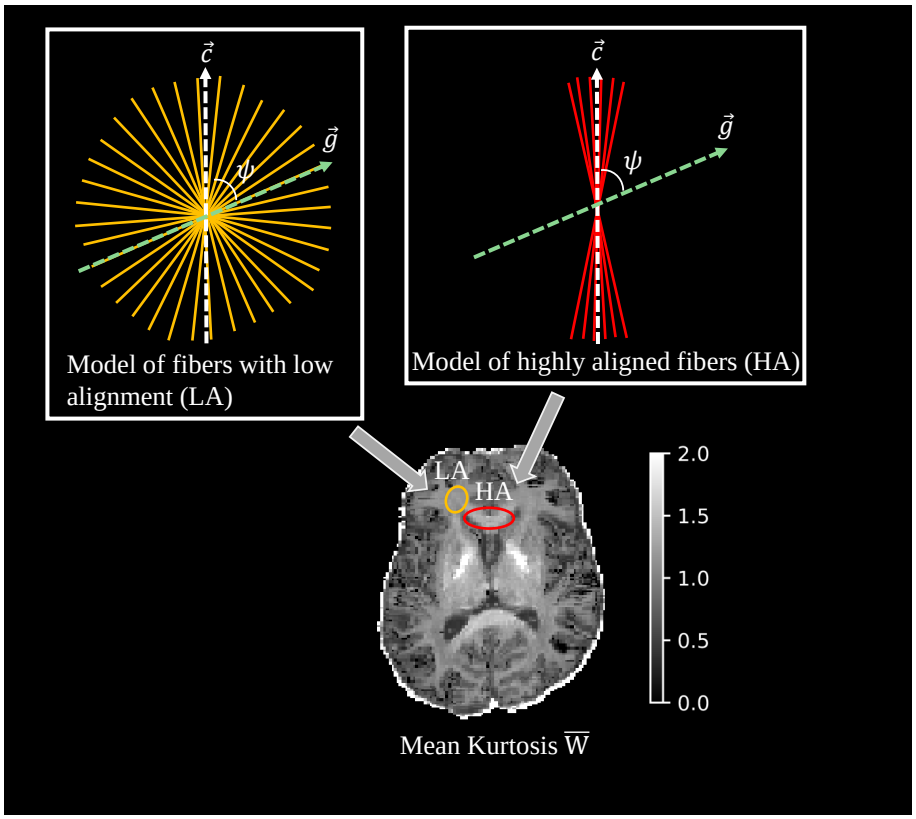

Fig. 2.4: Model of fiber alignment in characteristic areas of the brain. Left: in-vivo map of the mean kurtosis $\overline{W}$ with a typical area where fibers with low alignment (LA) are found and a typical area where fibers with high alignment (HA) are found. Right: the corresponding golden and red sticks depict an idealized model of the underlying fiber arrangement, the white dashed line indicates the axis of symmetry $\vec{c}$, the green dashed line indicates the diffusion gradient direction $\vec{g}$, ψ is the angle between $\vec{g}$ and $\vec{c}$.

MAPE was averaged per SNR across the 12 simulated voxels and the SNR above which this averaged MAPE $< 5\%$ is reported.

For simulation of the three synthetic voxels, the axis of symmetry $\vec{c} = (1, 0, 0)^T$ was fixed throughout the study. For data fitting, the two angles θ and ϕ that define the axis of symmetry within the axisymmetric DKI framework were variable but constrained to $\theta, \phi \in [-2\pi, 2\pi]$ which improved convergence of the fitting algorithm. Data were simulated according to the simulation scheme described in Section 2.6.

2.8 Diffusion signal profiles influenced by fiber alignment

To further elucidate differences between tissues with different levels of fiber alignment, angular signal profiles under the influence of noise were studied for the three voxels of the `synthetic dataset`. Noise-free and noise-contaminated signals have been simulated (SNR = 20). The simulated signal's mean and standard deviation could then be plotted as a function of angle ψ (in degree) between diffusion gradient $\vec{g}$ and axis of symmetry $\vec{c}$. For a graphical representation of angle ψ, see Figure 2.4.

3 Results

We first look at the results of the diffusion signal profiles in voxels with different levels of fiber alignments (Section 3.1) because these not only explain the results obtained in different tissues but also help to understand the difference between estimating the parallel or the perpendicular AxTM. After that, our main findings are stated and the corresponding results are reported (Section 3.2).

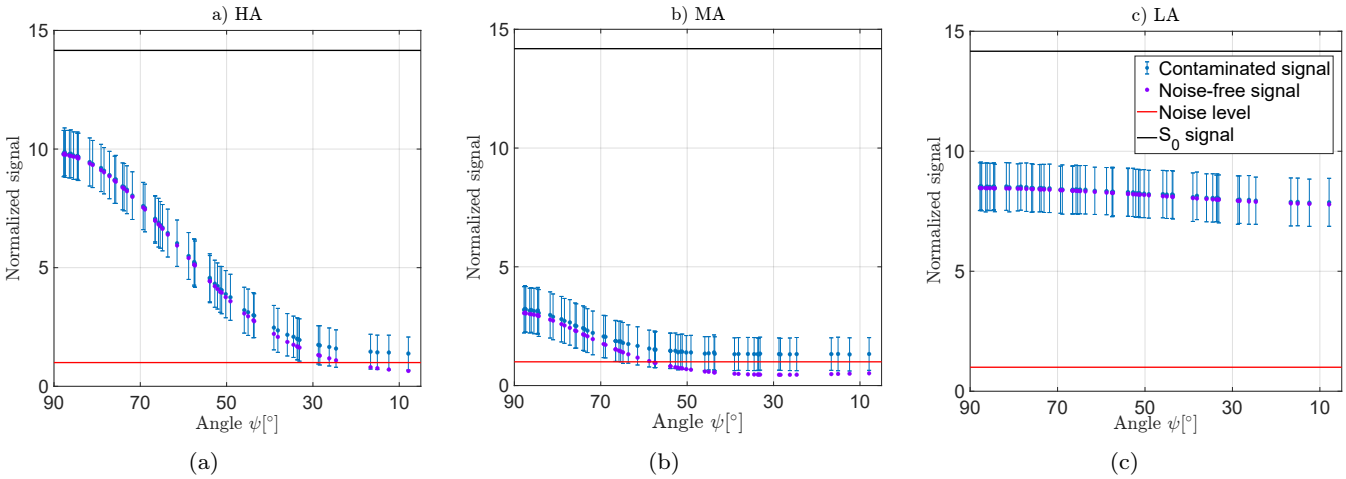

Fig. 3.1: Simulated signal decay at SNR $= \sqrt{2}\frac{S_0}{\sigma} = 20$ of the signal at $b = 0\frac{s}{mm^2}$ (S_0) corresponding to $\sigma = \sqrt{2}\frac{S_0}{20}$. Signal decay is shown for the `synthetic dataset` consisting of a) fibers with high alignment (HA), b) moderate alignment (MA) and c) low alignment (LA) as a function of angle ψ between the diffusion gradient $\vec{g}$ and the axis of symmetry $\vec{c}$, see Section 2.8. The "Contaminated signal" shows the mean and standard deviation over 2500 noise-samples. All signals, including the noise-free ones, were normalized to the noise strength, the plots always show $\frac{S}{\sigma}$. All three plots show the signals for the highest b-shell ($b = 2500\frac{s}{mm^2}$). For a graphical representation of angle ψ see Figure 2.4.

3.1 Diffusion signal profiles influenced by fiber alignment

Each of the simulated voxels of the `synthetic dataset` shows a characteristic, ψ dependent shape, see Fig. 3.1. For smaller angles ψ between $\psi = 20°$ and $\psi = 0°$, the simulated signals of white matter with highly fibers are strongly diffusion weighted and are close or below the noise floor (SNR $= 1$) where the signal and noise strength are equal, see Fig. 3.1a. In the simulated voxel of fibers with moderate alignment, the noise floor is already reached for angles $\psi \approx 50°$, see Fig. 3.1b. In the simulated voxel of white matter with low fiber alignment the noise floor is never reached and the simulation shows a seemingly constant, ψ independent signal form, see Fig. 3.1c. In summary, the signal in highly and moderately aligned fibers decays along the direction of symmetry, whereas there is almost no decay in fibers with low alignment.

3.2 Results of simulation study

Fig. 3.2 shows the SNRs required to accurately estimate the AxTM (MAPE$<$ 5%, Eq. (2.8)) in the `synthetic` and `in-vivo like dataset`. Shown are the results for axisymmetric DKI and standard DKI with (hatched) or without RBC.

RBC most effective in highly aligned fibers and parallel diffusion: RBC was most effective for the parallel parameters $D_\parallel$ and $W_\parallel$ in highly to moderately aligned fibers (for both the synthetic and `in-vivo like dataset`), see Fig. 3.2. For example, achieving MAPE $<$5% for $W_\parallel$ in the synthetic highly aligned fibers voxel could be reduced from SNR= 81 to SNR=25 (standard DKI) or SNR=29 (axisymmetric DKI). In the in-vivo like voxels, the SNR requirements for achieving MAPE $<$5% for $W_\parallel$ could be reduced from 20 to 10 (standard DKI) or to 8 (axisymmetric DKI). Estimation of $\overline{W}$ was significantly improved by RBC in the synthetic HA and MA voxels but only slightly in the `in-vivo like datasets`.

Superiority of axisymmetric DKI in fibers with low alignment where RBC is ineffective: In the synthetic LA voxel, estimation of $D_\parallel$, $D_\perp$, $W_\parallel$ and $W_\perp$ were substantially improved by using the axisymmetric DKI framework instead of standard DKI. E.g., it only required an SNR= 15 (axisymmetric DKI) instead of SNR= 51 (standard DKI) to achieve MAPE $<$5% for $W_\perp$. For $\overline{W}$, axisymmetric DKI performed slightly worse than standard DKI (SNR= 8 instead of SNR= 5). Interestingly, RBC did not influence the fitting results much in this fiber alignment configuration but even worsened them in some cases (e.g. $D_\parallel$), see Figure 3.2.

Axisymmetric DKI improves estimation of perpendicular parameters and RBC can also worsen

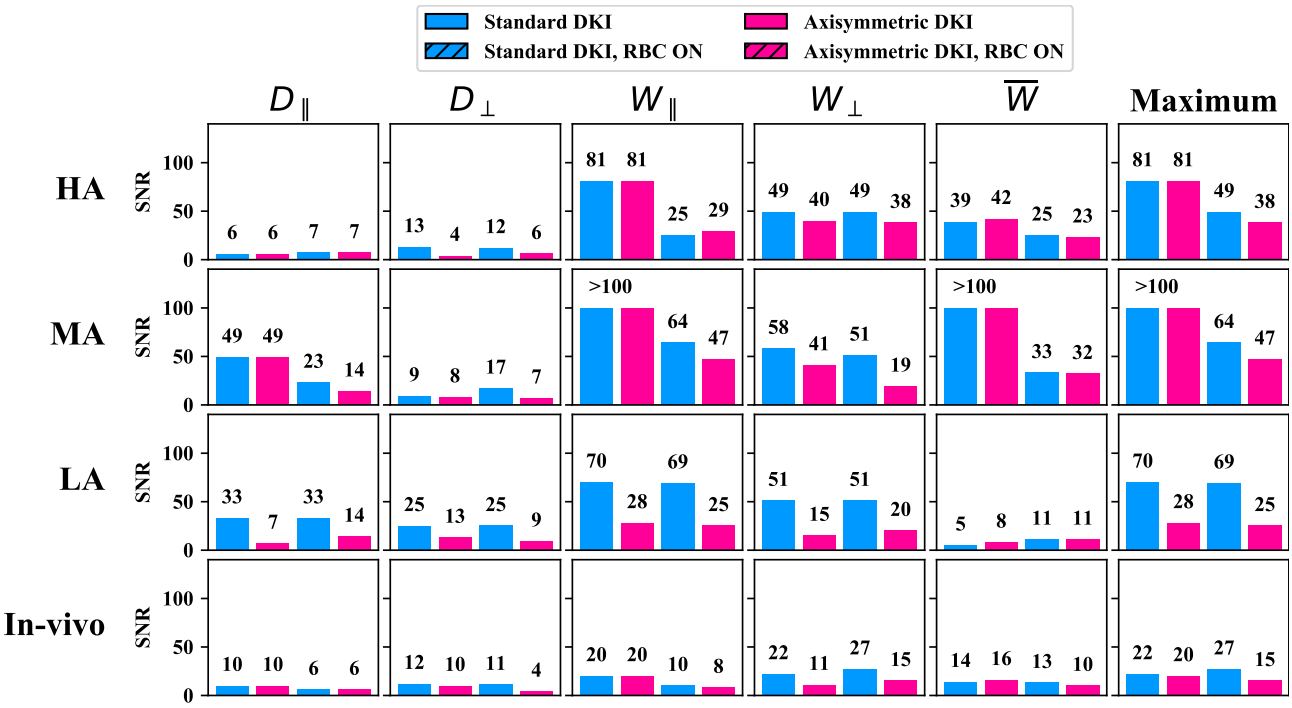

Fig. 3.2: Signal-to-noise ratio (SNR) above which the mean absolute percentage error (MAPE, Eq. (2.8)) $< 5\%$ for the `synthetic dataset` with high, medium and low fiber alignment ("HA", "MA", "LA") and the `in-vivo like dataset`. For the `in-vivo like dataset`, the MAPE was averaged across the 12 simulated voxels and the SNR above which this average MAPE $< 5\%$ is shown. The number above the barplots indicates the barplot's height. Blue encodes standard DKI, red encodes axisymmetric DKI, the hatched barplots show the results if RBC is used. "Maximum" shows the maximum SNR needed to achieve MAPE $< 5\%$ across all five AxTM.

accuracy: Estimation of $D_\perp$ and $W_\perp$ could also be improved (MAPE $<5\%$ reached for lower SNRs) by using the axisymmetric DKI framework in highly and moderately aligned fibers of the `synthetic` and `in-vivo like dataset` (e.g., for HA, $D_\perp$: SNR= 4 instead of SNR= 13; $W_\perp$: SNR= 40 instead of SNR= 49). Interestingly, there were also few scenarios in which RBC increased the SNR requirements. As described above this happened in the LA voxel and, other than that, predominantly for the perpendicular parameters, e.g., from SNR= 11 to SNR= 15 for the axisymmetric DKI fit of $W_\perp$ in the `in-vivo like dataset`.

4 Discussion

4.1 Summary of main findings

The axisymmetric DKI tensor metrics (AxTM) are the parallel and perpendicular diffusivity and kurtosis and the mean kurtosis. Fig. 2.1 shows the AxTM estimated for the in-vivo dataset of this study obtained with the axisymmetric DKI fit of the ACID toolbox. Rician bias correction (RBC) is highly effective for increasing estimation accuracy of the AxTM associated with diffusion parallel to the main fiber orientation, i.e., parallel diffusivity and kurtosis, in white matter with highly aligned fibers. In contrast, it fails in improving estimation accuracy in parameters perpendicular to the main fiber orientation or if fiber alignment is too low. For the latter scenarios, axisymmetric DKI is more effective than standard DKI. Overall, the combination of axisymmetric DKI with RBC was the best option for estimating all five AxTM, see "Maximum" column of Figure 3.2. This combination achieved a mean absolute percentage error (MAPE, Eq. (2.8)) $< 5\%$ on our simulated `in-vivo like data` if the signal-to-noise ratio (SNR)$\geq$ 15, making this combination a possibly valuable tool in neuroscience and clinical research studies.

4.2 Rician noise bias and its correction: Effectiveness for different DKI parameters and levels of fiber alignment within white matter

The effectiveness of RBC correlated with the severity of the Rician noise bias influenced by either the level

of fiber alignment or direction of the AxTM which indicates that the proposed method for RBC indeed mitigates Rician noise bias. Severity of the Rician noise bias is inversely proportional to the SNR and hence depends on a variety of parameters. One of these parameters is the level of water mobility which tunes the diffusivity and thereby the diffusion weighted signal. Water mobility is influenced by a combination of the level of fiber alignment and orientation of the AxTM relative to the axis of symmetry $\vec{c}$. Fig. 3.1 shows simulated signals in three tissue types with varying degrees of fiber alignment as a function of angle ψ between $\vec{c}$ and diffusion gradient $\vec{g}$. In highly aligned fibers for example, the diffusion signal is heavily diffusion weighted if measured along the main fiber orientation (small angle ψ) and the Rician noise bias in these signals therefore strongest, see Fig. 3.1a. Since the parallel AxTM ($D_\parallel$ and $W_\parallel$) predominantly depend on these signals, it can be expected that they, too, are more heavily biased in a high fiber alignment setting. Accordingly, we found that Rician bias correction (RBC) turned out to be particularly important for the AxTM associated with parallel diffusion ($D_\parallel$ and $W_\parallel$) in highly aligned white matter (`synthetic dataset` and `in-vivo like dataset`). On the other hand, diffusion perpendicular to $\vec{c}$ will be more restricted than the parallel diffusion and the SNR therefore higher. $D_\perp$ and $W_\perp$ should therefore be less affected by the Rician noise bias and we found that RBC was not as effective for the perpendicular parameters $D_\perp$ and $W_\perp$ in white matter with highly aligned fibers. However, RBC was very effective for $W_\perp$ in the dataset of white matter with fibers with moderate alignment in the `synthetic dataset`. This could be due to the relatively high perpendicular diffusivity of the MA voxel (Table 7.3) causing a strong diffusion weighting and therefore smaller perpendicular signal in this case (Fig. 3.1b).

RBC was furthermore ineffective in tissues with fibers that have low alignment, e.g., the "LA" voxel of the `synthetic dataset` where FA= 0.067, see Figure 3.2. Here, the signal change as a function of angle between $\vec{c}$ and $\vec{g}$ is smaller than the variation introduced by noise. This may lead to overfitting to the noise pattern, especially for the more complex standard DKI framework. Furthermore, the original signal shape may be lost in the noise pattern which is why RBC could even increase the bias instead of reducing it because it acts on a falsely modeled signal form. In fibers with low alignment, the signals almost seem independent of the diffusion gradient direction since these tissues do not posses a clearly distinguishable axis along which water mobility is significantly heightened compared to other directions, see Fig. 3.1c. For the same SNR (in reference to the S_0 signal), the Rician noise bias in such tissues is therefore less severe, compared to, e.g., signals in highly aligned fibers acquired for diffusion gradients parallel to the axis of symmetry. Accordingly, we found that RBC had little to no effect on parameter estimation in white matter with low fiber alignment.

4.3 Advantage of the axisymmetric DKI framework

In the introduction, we hypothesized that a reduction of the parameter space could make axisymmetric DKI more robust against the Rician noise bias. We observed that axisymmetric DKI predominantly improved accuracy of parameter estimation of the perpendicular AxTM $D_\perp$ and $W_\perp$ in both the `synthetic dataset` (HA and MA voxels) and the `in-vivo like dataset`, i.e., MAPE $< 5\%$ was achieved for lower SNRs. An increased noise-robustness in case of the perpendicular AxTM would make sense, because reduction of the parameter space is especially pronounced for these metrics. In standard DKI, 6 of the 22 framework parameters are needed to compute $W_\perp$ and 2 are needed to compute $D_\perp$, see Table 2.1. Axisymmetric DKI, on the other hand, always estimates these parameters directly. The reduction in SNR needed to achieve MAPE $< 5\%$ for $W_\perp$ when using the axisymmetric DKI framework is equal or greater than the reduction for $D_\perp$. This pattern matches the level of parameter reduction of $W_\perp$ and $D_\perp$ which is more pronounced for $W_\perp$ than for $D_\perp$. This argument does not hold for $\overline{W}$ because it is comprised of parameters used to compute both $W_\perp$ and $W_\parallel$ and the parallel parameters are more heavily affected by Rician noise, see Section 4.2. However, since the perpendicular AxTM are predominantly estimated from the "perpendicular signals" (see Section 4.2) which are less diffusion weighted in general, the influence of the Rician noise bias should be lower there. It is therefore unclear whether improvement is due to axisymmetric DKI reducing the Rician noise bias or if it is generally less susceptible to noise.

Furthermore, the accuracy of parameter estimation with axisymmetric DKI was substantially better in tissues with low fiber alignment (Figure 3.2) than with standard DKI. E.g., an SNR reduction of up to 70% when using axisymmetric DKI instead of standard DKI for estimation of $W_\perp$ in the LA voxel was observed, see Fig. 3.2. This could be due to the seemingly constant and consequent high signal independent of the diffusion gradient direction in fibers with low aligment when compared to the diffusion signal of fibers with high alignment. Since the variation in the almost constant

diffusion signal is dominated by noise, the complex 22 parametric standard DKI framework is more likely to overfit the data than the 8 parametric axisymmetric DKI framework, particularly in case of lower SNRs where noise has a greater impact. This could be the reason for the clear advantage of axisymmetric DKI over standard DKI in this fiber configuration.

4.4 Considerations

Looking at the estimation accuracy for each of the five AxTM individually revealed that each metric comes with different SNR requirements. Estimation of $W_{\|}$ with a MAPE$<$ 5%, for example, required an SNR of 81 in the HA voxel of the `synthetic dataset` and an SNR of $>$ 100 in the MA voxel of the `synthetic dataset` if RBC was not used. This reveals that current measurement protocols could reach their limits under realistic conditions where the SNR is below 81 or 100 if Rician bias correction is not used. This underlines the importance of using Rician bias correction in cases where all five AxTM are of importance, e.g., for estimation of the biophysical microstructure parameters.

Similar to previous simulation studies on RBC (Veraart et al., 2011, 2013a; André et al., 2014), we focused on the effects of RBC on the averaged estimated AxTM over the 2500 noise samples. The SNR at which the AxTM could be estimated with a MAPE $<$ 5% is reported for that ensemble average. Therefore, the reported results may not directly translate themselves one to one into in-vivo like applications where only one noise realization per voxel is measured.

5 Conclusion

Limited resources typically require a trade-off between MR-image acquisition time and image resolution, which affects the signal-to-noise ratio (SNR) in the acquired data. Our study revealed that even realistic measurement protocols can reach their limits if Rician bias correction (RBC) is not used. Certain fiber configurations required SNRs of more than 100 to estimate all of the five AxTM with a high accuracy without RBC. This demonstrates the importance of RBC in scenarios where precise knowledge of all five AxTM is required. Axisymmetric DKI with RBC has been demonstrated to be the most SNR effective choice for estimating the AxTM because of two mutually supporting factors. First, RBC itself is most effective for the parallel diffusivity and kurtosis and the mean kurtosis, however, it needs at least some level of fiber alignment to work. Second, compared to standard DKI, axisymmetric DKI is superior in fibers with low alignment and more effective for estimating the perpendicular diffusivity and kurtosis.

All of this makes the combination of axisymmetric DKI with RBC a possibly valuable tool for neuroscience and clinical research studies where a gain in SNR could either be used to reduce scan time or increase spatial resolution.

6 Availability of data and materials

The open source ACID toolbox for SPM contains the estimation methods for standard and axisymmetric DKI with and without Rician bias correction used in this study and is available at
http://www.diffusiontools.com/.

7 Funding

This work was supported by the German Research Foundation (DFG Priority Program 2041 "Computational Connectomics", [AL 1156/2-1;GE 2967/1-1; MO 2397/5-1; MO 2249/3–1], by the Emmy Noether Stipend: MO 2397/4-1) and by the BMBF (01EW1711A and B) in the framework of ERA-NET NEURON.

Acknowledgements

The Gauss Newton fit algorithm implementation used in this study was conceptualized and written by Jan Modersitzki and expanded by Lars Ruthotto who, e.g., implemented slice-wise parameter estimation and introduced an efficient, multi-voxel procedure to accelerate convergence; both improved the algorithm's run-time.

References

Aja-Fernández S, Tristán-Vega A (2012) Influence of noise correlation in multiple-coil statistical models with sum of squares reconstruction. Magnetic Resonance in Medicine 67(2):580–585

André ED, Grinberg F, Farrher E, Maximov II, Shah NJ, Meyer C, Jaspar M, Muto V, Phillips C, Balteau E (2014) Influence of noise correction on intra- and inter-subject variability of quantitative metrics in diffusion kurtosis imaging. PLoS ONE 9(4):e94531

Bunke H, Schmidt W (1980) Asymptotic results on nonlinear approximation of regression functions and weighted least squares. Series Statistics 11(1):3–22

Coelho S, Pozo JM, Jespersen SN, Jones DK, Frangi AF (2019) Resolving degeneracy in diffusion MRI biophysical model parameter estimation using double diffusion encoding. Magnetic Resonance in Medicine 82(1):395–410

Constantinides CD, Atalar E, McVeigh ER (1997) Signal-to-noise measurements in magnitude images from NMR phased arrays. Magnetic Resonance in Medicine 38(5):852–857

Coutu JP, Chen JJ, Rosas HD, Salat DH (2014) Non-Gaussian water diffusion in aging white matter. Neurobiology of Aging 35(6):1412–1421

Cox SR, Ritchie SJ, Tucker-Drob EM, Liewald DC, Hagenaars SP, Davies G, Wardlaw JM, Gale CR, Bastin ME, Deary IJ (2016) Ageing and brain white matter structure in 3,513 UK Biobank participants. Nature Communications 7(1)

Deppe M, Kellinghaus C, Duning T, Möddel G, Mohammadi S, Deppe K, Schiffbauer H, Kugel H, Keller SS, Ringelstein EB, Knecht S (2008) Nerve fiber impairment of anterior thalamocortical circuitry in juvenile myoclonic epilepsy. Neurology 71(24):1981–1985

Derek K Jones P (2012) Diffusion MRI Theory, Methods, and Applications: Theory, Methods, and Applications. Oxford University Press, Oxford

Donat CK, Yanez Lopez M, Sastre M, Baxan N, Goldfinger M, Seeamber R, Müller F, Davies P, Hellyer P, Siegkas P, Gentleman S, Sharp DJ, Ghajari M (2021) From biomechanics to pathology: predicting axonal injury from patterns of strain after traumatic brain injury. Brain 144(1):70–91

Eickhoff SB, Stephan KE, Mohlberg H, Grefkes C, Fink GR, Amunts K, Zilles K (2005) A new SPM toolbox for combining probabilistic cytoarchitectonic maps and functional imaging data. NeuroImage 25(4):1325–1335

Elliott LT, Sharp K, Alfaro-Almagro F, Shi S, Miller KL, Douaud G, Marchini J, Smith SM (2018) Genome-wide association studies of brain imaging phenotypes in UK Bioban. Nature 562(7726)

Genç E, Fraenz C, Schlüter C, Friedrich P, Hossiep R, Voelkle MC, Ling JM, Güntürkün O, Jung RE (2018) Diffusion markers of dendritic density and arborization in gray matter predict differences in intelligence. Nature Communications 9(1)

Glenn GR, Tabesh A, Jensen JH (2015) A simple noise correction scheme for diffusional kurtosis imaging. Magnetic Resonance Imaging 33(1):124–133

Gudbjartsson H, Patz S (1995) The Rician distribution of noisy MRI data. Magnetic Resonance in Medicine 34(6):910–914

Hansen B, Jespersen SN (2016) Data for evaluation of fast kurtosis strategies, b-value optimization and exploration of diffusion MRI contrast. Scientific Data 3(1):160072

Hansen B, Jespersen SN (2017) Recent developments in fast kurtosis imaging. Frontiers in Physics 5:40

Hansen B, Shemesh N, Jespersen SN (2016) Fast imaging of mean, axial and radial diffusion kurtosis. NeuroImage 142:381–393

Hansen B, Khan AR, Shemesh N, Lund TE, Sangill R, Eskildsen SF, Østergaard L, Jespersen SN (2017) White matter biomarkers from fast protocols using axially symmetric diffusion kurtosis imaging. NMR in Biomedicine 30(9):e3741

Henkelman RM (1985) Measurement of signal intensities in the presence of noise in MR images. Medical Physics 12(2):232–233

Jensen JH, Helpern JA (2003) Quantifying non-Gaussian water diffusion by means of pulsed-field-gradient MRI. Proceedings of ISMRM 2003, program number 2154

Jensen JH, Helpern JA, Ramani A, Lu H, Kaczynski K (2005) Diffusional kurtosis imaging: The quantification of non-Gaussian water diffusion by means of Magnetic Resonance Imaging. Magnetic Resonance in Medicine 53(6):1432–1440

Jespersen SN, Olesen JL, Hansen B, Shemesh N (2018) Diffusion time dependence of microstructural parameters in fixed spinal cord. NeuroImage 182:329–342

Karolis VR, Corbetta M, Thiebaut de Schotten M (2019) The architecture of functional lateralisation and its relationship to callosal connectivity in the human brain. Nature Communications 10(1):1417

Koay CG, Özarslan E, Basser PJ (2009) A signal-transformational framework for breaking the noise floor and its applications in MRI. Journal of Magnetic Resonance 197(2):108–119

Modersitzki J (2009) FAIR: Flexible Algorithms for Image Registration. SIAM, Philadelphia

Novikov DS, Veraart J, Jelescu IO, Fieremans E (2018) Rotationally-invariant mapping of scalar and orientational metrics of neuronal microstructure with diffusion MRI. NeuroImage 174:518 – 538

Polzehl J, Tabelow K (2016) Low SNR in Diffusion MRI Models. Journal of the American Statistical Association 111(516):1480–1490

Rice SO (1944) Mathematical analysis of random noise. Bell System Technical Journal 23(3):282–332

Rovira À, Wattjes MP, Tintoré M, Tur C, Yousry TA, Sormani MP, De Stefano N, Filippi M, Auger C,

Rocca MA, Barkhof F, Fazekas F, Kappos L, Polman C, Miller D, Montalban X, on behalf of the MAGNIMS study group (2015) MAGNIMS consensus guidelines on the use of MRI in multiple sclerosis—clinical implementation in the diagnostic process. Nature Reviews Neurology 11(8):471–482

Sijbers J, den Dekker A, Scheunders P, Van Dyck D (1998) Maximum-likelihood estimation of Rician distribution parameters. IEEE Transactions on Medical Imaging 17(3):357–361

Tabesh A, Jensen JH, Ardekani BA, Helpern JA (2011) Estimation of tensors and tensor-derived measures in diffusional kurtosis imaging. Magnetic Resonance in Medicine 65(3):823–836

Veraart J, Hecke WV, Sijbers J (2011) Constrained maximum likelihood estimation of the diffusion kurtosis tensor using a Rician noise model. Magnetic Resonance in Medicine 66(3):678–686

Veraart J, Rajan J, Peeters RR, Leemans A, Sunaert S, Sijbers J (2013a) Comprehensive framework for accurate diffusion MRI parameter estimation. Magnetic Resonance in Medicine 70(4):972–984

Veraart J, Sijbers J, Sunaert S, Leemans A, Jeurissen B (2013b) Weighted linear least squares estimation of diffusion MRI parameters: Strengths, limitations, and pitfalls. NeuroImage 81:335–346, DOI 10.1016/j.neuroimage.2013.05.028, URL https://www.sciencedirect.com/science/article/pii/S1053811913005223

Supplementary material

7.1 Ground truth DKI datasets

Table 7.1: Ground truth in-vivo like standard DKI voxels for the `in-vivo like dataset` (Figure 2.3), shown are the diffusion and kurtosis tensor components and S_0, the diffusivities are in $[\frac{\mu m^2}{ms}]$.

Parameter	cb Dataset 1	cb Dataset 2	cb Dataset 3	ct Dataset 1	ct Dataset 2	ct Dataset 3
D_{11}	1.92726	1.62057	1.86790	0.53951	0.78384	0.73087
D_{22}	0.31583	0.38127	0.41435	0.36193	0.42447	0.49957
D_{33}	0.39808	0.39813	0.36425	1.54966	1.37428	1.29096
D_{12}	−0.00731	−0.26198	−0.11110	−0.15777	−0.08699	−0.05191
D_{13}	0.04079	−0.25240	0.09536	0.00094	−0.08181	−0.03291
D_{23}	0.03170	−0.09149	−0.03971	−0.04121	0.15430	0.03331
S_0	1.00000	1.00000	1.00000	1.00000	1.00000	1.00000
W_{1111}	4.26728	4.20207	3.73642	0.58735	1.16398	1.12725
W_{2222}	0.30183	0.43656	0.36961	0.22285	0.51330	0.74976
W_{3333}	0.43632	0.59204	0.26940	3.41702	2.14949	2.30314
W_{1112}	−0.15654	−0.41618	−0.18526	−0.07888	−0.06150	−0.08996
W_{1113}	0.10051	−0.64422	0.18910	0.00636	−0.02166	0.02767
W_{2221}	0.19206	−0.46340	−0.26578	−0.08910	−0.06061	−0.09517
W_{2223}	0.06537	−0.17548	−0.08403	0.09611	0.10937	−0.04710
W_{3331}	−0.08171	−0.15145	0.12274	−0.08214	−0.17008	−0.09078
W_{3332}	0.07430	−0.16995	−0.09129	−0.12567	0.28125	−0.09293
W_{1122}	0.45163	0.51896	0.50221	0.20913	0.21167	0.25976
W_{1133}	0.45000	0.53712	0.43661	0.52253	0.56751	0.30986
W_{2233}	0.15867	0.16724	0.07048	0.32234	0.42040	0.39227
W_{1123}	−0.00501	−0.08834	−0.03636	0.07669	0.03705	−0.00512
W_{2213}	−0.00262	0.00521	0.08195	−0.02098	−0.08206	−0.02479
W_{3312}	0.03732	−0.13410	−0.11029	−0.16710	−0.06077	−0.02733
Parameter	or Dataset 1	or Dataset 2	or Dataset 3	slf Dataset 1	slf Dataset 2	slf Dataset 3
D_{11}	1.06085	0.67273	0.69468	0.46699	0.68565	0.63911
D_{22}	0.59047	0.75000	1.79639	0.43803	0.48026	0.61127
D_{33}	1.36088	1.48673	0.49756	1.69614	1.23269	1.22297
D_{12}	0.12149	0.04143	−0.43159	0.05648	0.02784	0.08187
D_{13}	0.61736	0.22247	0.19896	0.07981	−0.07817	−0.04450
D_{23}	0.05184	0.26023	−0.21783	−0.20355	−0.15512	−0.09252
S_0	1.00000	1.00000	1.00000	1.00000	1.00000	1.00000
W_{1111}	1.18421	0.74417	0.60364	0.38485	1.27168	0.65976
W_{2222}	0.48582	0.71486	2.21601	0.51498	0.72106	0.83091
W_{3333}	1.72750	1.99702	0.37346	3.25042	2.56281	1.96113
W_{1112}	0.09557	0.04945	−0.18369	0.03519	0.11477	0.00824
W_{1113}	0.42320	0.11965	0.04012	0.01711	0.05484	0.06571
W_{2221}	0.22072	−0.01878	−0.49678	0.11049	−0.03851	−0.10122
W_{2223}	0.13593	−0.00500	−0.40378	−0.02510	0.06858	0.06213
W_{3331}	0.70421	0.13580	0.03943	0.15730	−0.32397	−0.13608
W_{3332}	0.15332	0.36637	0.09475	−0.41687	−0.24668	−0.29428
W_{1122}	0.19154	0.25614	0.52836	0.12737	0.22065	0.18565
W_{1133}	0.61697	0.26980	0.15419	0.49145	0.36651	0.53366
W_{2233}	0.26455	0.40726	0.34763	0.42856	0.14162	0.27141
W_{1123}	0.04012	0.00642	−0.11345	−0.04016	−0.01867	−0.08256
W_{2213}	0.06872	0.07859	0.24902	−0.01085	−0.04099	0.02417
W_{3312}	0.02283	0.04014	−0.03715	0.06156	0.07493	0.17797

Table 7.2: Ground truth AxTM of the `in-vivo like dataset`, corresponding to the tensor components listed in Table 7.1, the diffusivities are in $[\frac{\mu m^2}{ms}]$.

Voxel	$D_{\parallel}$	$D_{\perp}$	$W_{\parallel}$	$W_{\perp}$	$\overline{W}$
cb voxel 1	1.928	0.356	4.276	0.401	1.425
cb voxel 2	1.714	0.343	4.549	0.387	1.535
cb voxel 3	1.883	0.382	3.798	0.240	1.279
ct voxel 1	1.551	0.450	3.427	0.471	1.267
ct voxel 2	1.413	0.585	2.373	0.762	1.245
ct voxel 3	1.295	0.613	2.294	0.903	1.221
or voxel 1	1.857	0.578	2.891	0.463	1.109
or voxel 2	1.623	0.643	2.244	0.706	1.064
or voxel 3	1.995	0.497	2.959	0.498	1.051
slf voxel 1	1.732	0.435	3.421	0.439	1.249
slf voxel 2	1.275	0.562	2.715	0.919	1.203
slf voxel 3	1.242	0.616	2.153	0.725	1.087

Table 7.3: Set of synthetic AxTM, S_0 and axis of symmetry $\vec{c}$ used to simulate the `synthetic dataset` based on axisymmetric DKI. The `synthetic dataset` consisting of three voxels with sets of $\{D_{\parallel}, D_{\perp}, W_{\parallel}, W_{\perp}, \overline{W}\}$ was taken from Coelho et al. (2019), diffusivities are in $[\frac{\mu m^2}{ms}]$, S_0 is in arbitrary units.

Dataset	$D_{\parallel}$	$D_{\perp}$	$W_{\parallel}$	$W_{\perp}$	$\overline{W}$	S_0	$\vec{c}$
Fibers with high alignment (HA)	1.503	0.195	1.456	0.291	0.926	1	$(1,0,0)^T$
Fibers with moderate alignment (MA)	1.557	1.048	0.396	0.708	0.330	1	$(1,0,0)^T$
Fibers with low alignment (LA)	0.457	0.408	2.901	2.702	2.770	1	$(1,0,0)^T$